

Cite this: *Phys. Chem. Chem. Phys.*, 2012, **14**, 14010–14022

www.rsc.org/pccp

PAPER

Identifying active surface phases for metal oxide electrocatalysts: a study of manganese oxide bi-functional catalysts for oxygen reduction and water oxidation catalysis†

Hai-Yan Su,^a Yelena Gorlin,^b Isabela C. Man,^a Federico Calle-Vallejo,^a
Jens K. Nørskov,^{bc} Thomas F. Jaramillo^{*b} and Jan Rossmeisl^{*a}

Received 16th March 2012, Accepted 23rd August 2012

DOI: 10.1039/c2cp40841d

Progress in the field of electrocatalysis is often hampered by the difficulty in identifying the active site on an electrode surface. Herein we combine theoretical analysis and electrochemical methods to identify the active surfaces in a manganese oxide bi-functional catalyst for the oxygen reduction reaction (ORR) and the oxygen evolution reaction (OER). First, we electrochemically characterize the nanostructured α - Mn_2O_3 and find that it undergoes oxidation in two potential regions: initially, between 0.5 V and 0.8 V, a potential region relevant to the ORR and, subsequently, between 0.8 V and 1.0 V, a potential region between the ORR and the OER relevant conditions. Next, we perform density function theory (DFT) calculations to understand the changes in the MnO_x surface as a function of potential and to elucidate reaction mechanisms that lead to high activities observed in the experiments. Using DFT, we construct surface Pourbaix and free energy diagrams of three different MnO_x surfaces and identify $1/2$ ML HO^* covered Mn_2O_3 and O^* covered MnO_2 , as the active surfaces for the ORR and the OER, respectively. Additionally, we find that the ORR occurs through an associative mechanism and that its overpotential is highly dependent on the stabilization of intermediates through hydrogen bonds with water molecules. We also determine that OER occurs through direct recombination mechanism and that its major source of overpotential is the scaling relationship between HOO^* and HO^* surface intermediates. Using a previously developed Sabatier model we show that the theoretical predictions of catalytic activities match the experimentally determined onset potentials for the ORR and the OER, both qualitatively and quantitatively. Consequently, the combination of first-principles theoretical analysis and experimental methods offers an understanding of manganese oxide oxygen electrocatalysis at the atomic level, achieving fundamental insight that can potentially be used to design and develop improved electrocatalysts for the ORR and the OER and other important reactions of technological interest.

1. Introduction

Fundamental understanding of electrochemical reactions on surfaces has improved significantly in recent years, yet many

microscopic processes occurring during electrochemical reactions are still poorly understood due to difficulties in simulating electrochemical reactions computationally and in pinpointing active sites experimentally. The ultimate challenge in electrocatalyst development is to identify the active sites on a given catalytic surface and determine the reaction mechanisms on those sites. If one can achieve such level of fundamental understanding, one could accelerate the design and development of improved electrocatalysts.^{1–5}

The electrochemical oxygen reduction reaction (ORR) and oxygen evolution reaction (OER) are of great interest as they are processes involved in energy conversion between fuel and electricity and *vice versa*. The development of a bi-functional catalyst for both reactions is an important challenge in electrochemistry; such a catalyst could be particularly useful for energy storage applications. For example, the catalyst could be employed in a unitized regenerative fuel cell (URFC), which is

^a Center for Atomic-Scale Materials Design (CAMD), Department of Physics, DTU, Technical University of Denmark, DK-2800 Kgs. Lyngby, Denmark. E-mail: jross@fysik.dtu.dk

^b Department of Chemical Engineering, 381 North-South Mall, Stanford University, Stanford, CA 94305–5025, USA. E-mail: jaramillo@stanford.edu

^c SLAC National Accelerator Laboratory, Stanford, CA 94025-7015, USA

† Electronic supplementary information (ESI) available: (1) The phase-diagram of MnO_x surfaces calculated as a function of the potential at pH = 0; (2) free-energy diagram for oxygen reduction and oxygen evolution on all the non-self-consistent MnO_x surfaces; (3) the method to calculate the number of O (N_{O}) coordinated with Mn on various MnO_x surfaces; (4) the method to construct Pourbaix diagram for both bulk and surface. See DOI: 10.1039/c2cp40841d

an energy storage device that can utilize intermittent renewable energy such as wind or solar. During operation, a URFC splits water into H_2 and O_2 , in the electrolysis mode and consumes H_2 to produce electricity, in the fuel cell mode.^{6,7} Both the fuel cell reaction and the water electrolysis reaction require large overpotentials at the oxygen electrode – no current catalyst material operates near the equilibrium potential for either the ORR or the OER. Consequently, improved oxygen electrode catalysts will increase the efficiency of the full conversion cycle from electricity to hydrogen and back to electricity in an URFC.^{8,9} Furthermore, it is desirable to develop highly active catalysts from cheap and abundant materials, *i.e.* alternatives to IrO_2/Pt or IrO_2-RuO_2/Pt catalysts, which are the best catalysts known for these reactions.^{10–12}

In this study, we investigate ORR/OER catalytic activity of manganese oxides (MnO_x) surfaces. Several characteristics of MnO_x motivate our study: (1) Mn changes oxidation states from +2 to +3 to +4 near the equilibrium potential for the ORR and the OER,¹³ suggesting that Mn can exchange oxygen atoms with the electrolyte at relevant potentials – a property that could potentially facilitate ORR and OER chemistry, (2) manganese is an inexpensive, earth-abundant element, and thus is scalable for large-scale energy applications, and (3) there is precedent for Mn oxides effectively catalyzing the OER: the Oxygen-Evolving Complex (OEC) in Photosystem II is a Mn-oxo cluster that catalyzes the OER during photosynthesis.^{14–17} Historically, a number of manganese oxides have shown promising electrocatalytic activity for either the ORR or the OER, but not for both.^{18–30} Recently, it was shown that a nanostructured $\alpha-Mn_2O_3$ exhibited excellent bi-functional ORR and OER activity similar to that of the best known precious metal nanoparticle catalysts: Pt, Ru, and Ir.³¹ However, the bi-functional ORR/OER activities of the nanostructured $\alpha-Mn_2O_3$ and precious metal nanoparticles are still short of an ideal reversible oxygen electrode.

In principle, it should be possible to develop an ideal reversible oxygen electrode – a material that effectively catalyzes both the ORR and the OER. With such a catalyst, one would be able to obtain a high reduction current at potentials just cathodic of the equilibrium potential and a high anodic current at potentials just anodic of the equilibrium potential. Such a catalyst would likely undergo minimal changes in surface structure, swinging from one reaction to the other, as it would always operate near the equilibrium potential. For imperfect catalysts, there are large overpotentials associated with both the ORR and the OER, which means that the two reactions operate at significantly different potentials away from equilibrium in opposite directions. The different operating conditions will likely result in different surface conditions within each potential window of activity and likely different oxidation states of the catalyst surface at the relevant potentials for the ORR and the OER.

To understand surface conditions of imperfect catalysts under ORR/OER relevant potentials, a variety of *in situ* and *ex situ* spectroscopic techniques have been employed.^{25,32–35} We believe that density functional theory (DFT) calculations can also be used to help elucidate active catalyst surfaces. While DFT methods have problems describing transition metal oxides accurately, they have been shown recently to

describe trends in reactivity of metals and metal oxides for the OER and the ORR quite well.^{36–40} Due to the complexity of the systems of interest in describing these processes, DFT calculations are the only methods available to us at the moment. The calculations can be used to construct surface Pourbaix diagrams, which describe surface oxidation and dissolution processes at a given pH and potential,⁴¹ making it possible to identify thermodynamically stable surface phases during reaction conditions (as a function of pH and potential), the catalytic activity of those surfaces, and the associated mechanistic pathways for the reactions of interest. The knowledge of active surfaces and reaction mechanisms gained from DFT studies will shed light onto the surface chemistry of catalyst materials in ways that are extremely difficult to obtain with modern experimental tools. DFT can thus play a unique role in contributing to the design and development of improved materials.

In the work described herein, we present DFT calculations in combination with electrochemical characterization to elucidate the active surfaces and reaction mechanisms for the ORR and the OER on a bi-functional Mn oxide catalyst. First, the electrochemical characterization of a recently developed nanostructured manganese oxide catalyst demonstrates excellent ORR and OER activity, but suggests that the catalyst undergoes a change in the oxidation state in the onset region of ORR activity as well as in the potential region between ORR and OER activity. Attempts to characterize the surface oxidation state under operating conditions using *ex situ* X-ray photoelectron spectroscopy have yielded some information on the active surfaces involved.³⁵ To gain greater insight into the surface chemistry of this catalyst during reaction conditions, we turn to DFT calculations to identify the precise surface structures involved as well as associated reaction mechanisms for both oxygen reduction and oxygen evolution.

Our study involves the following elements. The first step is to determine which surface structures of manganese oxide are present as a function of pH and applied potential *versus* the reversible hydrogen electrode (RHE). We obtain this information by employing DFT calculations to generate surface Pourbaix diagrams for different adsorbate (*e.g.* O^* and HO^*) covered surfaces. To link the calculated surface structures of manganese oxide to ORR or OER conditions, we then use DFT to calculate binding energies for all reaction intermediates involved in the ORR and the OER and predict ORR and OER overpotentials for each surface structure. These overpotentials are then inserted into the previously developed Sabatier model⁴² to produce a computationally derived linear sweep voltammogram (LSV). The computationally derived LSV reveals activity as a function of applied potential for manganese oxide surfaces in a self-consistent manner, meaning that reaction turnover can only occur on surface phases that are identified to be present at a given potential. Our results indicate that the active surface for the ORR is 1/2 ML HO^* covered Mn_2O_3 and for the OER, O^* covered MnO_2 . Having identified the active surfaces involved in these reactions, our DFT calculations can offer further insight into mechanistic pathways: the associative mechanism is the expected pathway for the ORR pathway on 1/2 ML HO^* covered Mn_2O_3 and the direct recombination mechanism is the most likely OER pathway on O^* covered MnO_2 .

When the computationally derived LSV is compared to the experimental LSV measured on a recently developed nano-structured manganese oxide catalyst, the theoretical predictions closely match experimental onsets for ORR and OER catalytic activities. The close match between theory and experiment validates the application of a first-principles theoretical analysis to the electrochemical oxygen reduction and oxygen evolution reactions on surfaces at the atomic level. By focusing our analysis on reaction energetics, namely the binding energies of reactive intermediates, we expect our approach to be robust and not very dependent on the computational setup and the exchange and correlation functional applied in the DFT simulations.

2. Methods

2.1 Computational methods

The spin-polarized DFT calculations are performed at the generalized gradient approximation (GGA) RPBE level⁴³ using the plane wave implementation in Dacapo and the Atomic Simulation Environment Ultra-soft pseudo-potentials are used to deal with the ion cores.⁴⁴ Therefore the electronic wave-functions can be represented well by a plane wave basis set with a cutoff energy of 350 eV. The electron density is treated on a grid corresponding to a plane wave cutoff at 500 eV. A Fermi smearing of 0.1 eV and Pulay mixing are used to ensure the fast convergence of the self-consistent electron density. Atomic positions are relaxed until the sum of the absolute forces is less than $0.05 \text{ eV } \text{\AA}^{-1}$. For reference, the calculated equilibrium lattice constants of MnO_x are $4.5 \text{ \AA}/\text{MnO}$, 5.78 \AA (a), 9.59 \AA (c)/ Mn_3O_4 , $9.51 \text{ \AA}/\alpha\text{-Mn}_2\text{O}_3$ and 4.43 \AA (a), 2.86 \AA (c)/ $\beta\text{-MnO}_2$, in good agreement with the experimental measurements and previous DFT studies.^{45–53}

The starting point for this analysis is calculations on four well-defined manganese oxide surfaces (Fig. 1). For the OER and the ORR it is likely that the facets control surface activity rather than surface defects since defects are expected to be covered by oxygen at the very oxidizing conditions relevant for OER and ORR. In this work, we specifically consider four close packed MnO_x surfaces⁴⁶ and examine their trends in behavior: $\text{MnO}(001)$, $\beta\text{-MnO}_2(110)$, $\text{Mn}_3\text{O}_4(100)$ and $\alpha\text{-Mn}_2\text{O}_3(110)$. The surface structures with the most stable terminations are shown in Fig. 1. For Mn_3O_4 (in Fig. 1a) all the surface Mn atoms are equivalent and each Mn atom coordinates with four oxygen atoms in the same plane and one oxygen in the second layer (see Fig. 1a). The $\alpha\text{-Mn}_2\text{O}_3(110)$ surface has four different types of Mn atoms (Fig. 1b): two Mn atoms coordinate with five oxygen atoms: four oxygen atoms in the same plane and one in the second layer (site 1), and three oxygen atoms in the same plane and two in the second layer (site 4). The other two atoms coordinate with four oxygen atoms: three oxygen atoms in the same plane and one oxygen in the second layer (site 2), and two oxygen atoms in the same plane and two in the second layer (site 3). $\beta\text{-MnO}_2$ has a rutile phase^{54,55} and two types of Mn atoms on the surface: five-coordinated Mn (coordinated unsaturated site, site 1 in Fig. 1c), with four oxygens in the same plane and one in the second layer, and six-coordinated Mn (bridge site, site 3 in Fig. 1c) that is

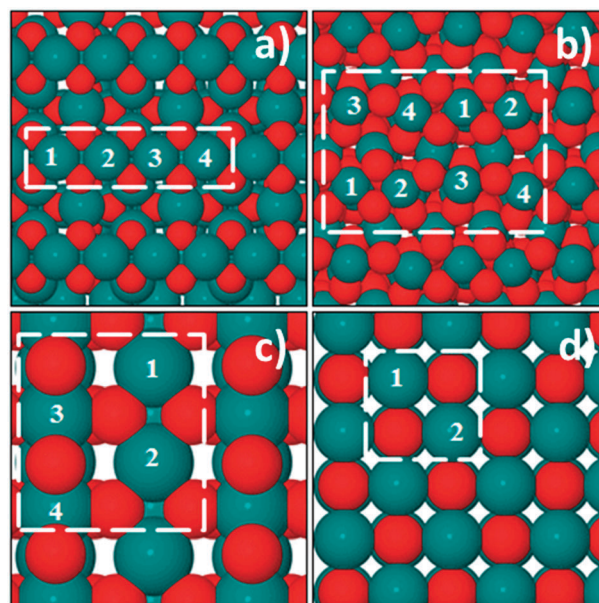


Fig. 1 The schematic structures (top view) of different manganese oxide phases, Mn atoms in blue, O atoms in red. (a) $\text{Mn}_3\text{O}_4(001)$ – white rectangle indicates the (2×1) unit cell with the equivalent five-fold coordinated active sites 1,2,3,4; (b) $\alpha\text{-Mn}_2\text{O}_3(110)$ white rectangle indicates the (1×1) unit cell with four types of sites: 1 – five-fold coordinated (with four oxygen atoms in the same plane), 4 – five-fold coordinated (three oxygen atoms in the same plane and two in the second layer), 2 – four-fold coordinated (three oxygen atoms in the same plane and one in the second layer) and 3 – four-fold coordinated (two oxygen atoms in the same plane and two in the second layer), and (c) $\text{MnO}_2(110)$ surfaces – a rutile type stoichiometric surface. The dashed line indicates a (1×2) unit cell. Positions 1 and 2 are equivalent and represent the active sites (cus). Sites 3 and 4 are equivalent six-fold coordinated and are called the bridge sites; (d) $\text{MnO}(100)$ with (1×1) unit cell. 1 and 2 are equivalent five-fold coordinated active sites.

considered to be the inactive sites. Our calculations show that the $\text{MnO}(001)$ surface (Fig. 1d) reconstructs immediately in the presence of oxygen, and thus this oxide phase is not considered any further.

A periodically repeating 4–8 layer slab is employed in the model to determine the most stable MnO_x surfaces in our calculations (see Fig. 1). A vacuum of at least 20 \AA is used to separate the slab from its periodic images. Supercells with periodicity (2×1) have been employed to simulate adsorption and electrochemical reaction, with Monkhorst–Pack type of k -point sampling of $4 \times 4 \times 1$ for $\text{MnO}(100)$ and $\beta\text{-MnO}_2(110)$, and $2 \times 4 \times 1$ for $\text{Mn}_3\text{O}_4(001)$. For the complex crystal structure of $\alpha\text{-Mn}_2\text{O}_3(110)$, only (1×1) unit cell and $2 \times 3 \times 1$ Monkhorst–Pack type of k -point sampling are used. The 2–4 top layers as well as possible adsorbates are fully relaxed.

We apply a previously developed method, the computational standard hydrogen electrode (CSHE) for modeling the thermochemistry of electrochemical reactions.^{37,38} In this method the only way the potential affects the relative free energy is through the chemical potential of the electrons in the electrode. This “first order” inclusion of the potential has been used to predict the activity trends for the ORR on metal and metal alloys and in the design of electrocatalysts.^{36,37} Furthermore, we have shown that thermochemical features such as phase diagrams in water are also well described by

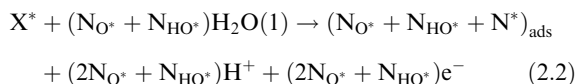
this method.⁵⁶ The only effect of the pH is the change of chemical potential of the solvated protons. At standard conditions (pH = 0), $\text{H}^+(\text{aq}) + \text{e}^-$ is in equilibrium with $1/2 \text{H}_2(\text{g})$ at zero potential vs. the SHE. At finite pH and potential vs. SHE (U_{SHE}) the chemical potential of a proton and an electron is:

$$(\text{H}^+(\text{aq})) + (\text{e}^-) = 1/2 \text{H}_2(\text{g}) - eU_{\text{SHE}} + k_{\text{B}}T \ln_{10} \text{pH} \quad (2.1)$$

2.2 Pourbaix diagrams

To construct the surface Pourbaix diagram for the MnO_x system, we first generate a calculated bulk Pourbaix diagram by considering the equilibrium between different bulk oxide phases and bulk manganese metal. In the same diagram we also include the equilibrium between different soluble products and solid substances. As we start by exploring phase behaviour in the bulk, all these values can be adapted from the Pourbaix atlas, the reference system is the bulk metallic phase.¹³ More details on the construction of the diagrams can be found in the ESI.† After constructing bulk Pourbaix diagrams which are equivalent to the diagrams found in the Pourbaix atlas, we go one step further and identify the adsorbates (e.g. O^* or HO^*) that are present and their coverage (e.g. $1/4 \text{ ML}$, $1/2 \text{ ML}$, etc.). We thus identify the most stable surface structures for each oxide phase at respective pH and potential, key information that is not found in the Pourbaix atlas. The calculations employed to determine the stable surfaces as a function of pH and potential employ a previously developed model.⁴¹ In short, the surface is in equilibrium with protons and liquid water at 298 K so that oxygen and hydroxyl may be exchanged between the surface and a reference electrolyte.

Consider a clean surface with a quantity of X^* available sites onto which oxygen or hydroxyl can potentially adsorb. At a given pH and potential, the surface will interact with the interfacial water layer such that some of the H_2O molecules at the interface will dissociate onto available sites, producing adsorbed O or HO and releasing protons and electrons in the process. We introduce the variables N_{O^*} and N_{HO^*} to reflect the number of adsorbed O and HO species, respectively, and the variable N^* which represents the number of remaining free sites at the given pH and potential after the adsorption processes have occurred. Thus, the total number of available sites to begin with, $\text{X}^* = N_{\text{O}^*} + N_{\text{HO}^*} + N^*$, i.e. after adsorption sites either contain O, HO, or remain free sites. The stoichiometric equation reflecting this process is as follows:



We can thus calculate the free energy change of the surface covered with adsorbates relative to the clean surface, on the DFT scale as follows:

$$\begin{aligned} G_{\text{surf}} &= E_{(\text{N}_{\text{O}^*} + \text{N}_{\text{HO}^*} + \text{N}^*)_{\text{ads}}}^{\text{DFT}} - E_{\text{X}^*}^{\text{DFT}} - (\text{N}_{\text{O}^*} + \text{N}_{\text{HO}^*})E_{\text{H}_2\text{O}(\text{g})}^{\text{DFT}} \\ &+ \frac{(2\text{N}_{\text{O}^*} + \text{N}_{\text{HO}^*})}{2}E_{\text{H}_2(\text{g})}^{\text{DFT}} + \Delta\text{ZPE} - T\Delta S \\ &- (2\text{N}_{\text{O}^*} + \text{N}_{\text{HO}^*})(eU - k_{\text{B}}T \ln a_{\text{H}^+}) \end{aligned} \quad (2.3)$$

where $E_{(\text{N}_{\text{O}^*}, \text{N}_{\text{HO}^*}, \text{N}^*)}^{\text{DFT}}$, $E_{\text{X}^*}^{\text{DFT}}$, $E_{\text{H}_2\text{O}(\text{g})}^{\text{DFT}}$, $E_{\text{H}_2(\text{g})}^{\text{DFT}}$ are the calculated ground state energies of the surface with the adsorbates, of the clean surface and of the reference molecules in the gas phase. Zero point energies (ZPE) corrections are calculated using DFT calculations of the vibrational frequencies and standard tables of molecules. The changes in entropy (TS^0 , $T = 298 \text{ K}$) are calculated from the standard tables for gas phase molecules.⁵⁷ Detailed description about how to perform all corrections can be found in ref. 37 and 38.

2.3 Experimental methods

The electrochemical characterization was performed on $\alpha\text{-Mn}_2\text{O}_3$ nanostructured thin films electrodeposited onto polished glassy carbon disks (GC, 0.196 cm^2 , SigradurG HTW Hochtemperatur-Werkstoffe GmbH) as described previously.³¹ The films were characterized using cyclic voltammetry (CV) in a three electrode electrochemical cell in a rotating disk electrode (RDE, Pine Instruments) configuration. All CVs were iR-compensated and measured using a Bio-Logic potentiostat (VMP3) in 0.1 M KOH electrolyte, in nitrogen or oxygen saturated environments, with a scan rate of 5 mV s^{-1} and a rotation rate of 1600 rpm . Platinum wire was used as a counter electrode and Hg/HgO electrode was used as a reference electrode. The potential scale was calibrated to a reversible hydrogen electrode (RHE) and all potentials are reported vs. RHE. CVs in nitrogen were used to identify oxidation state changes in an inert environment, while CVs in oxygen identified potentials relevant for the ORR and the OER. Base CVs in nitrogen and ORR CVs in oxygen were performed from 0.05 V to 1.1 V vs. RHE, while OER linear sweep voltammograms (LSV) were performed from 0.05 V to 1.9 V vs. RHE.

To compare ORR and OER activities of the nanostructured $\alpha\text{-Mn}_2\text{O}_3$ to active precious metals and metal oxides, electrochemical characterization was also performed on commercial carbon-supported platinum (20 wt\% Pt/C , Etek) and ruthenium (20 wt\% Ru/C , Premetek) nanoparticles which were previously shown to have a comparable surface area to the nanostructured $\alpha\text{-Mn}_2\text{O}_3$.³¹ Catalyst dispersions of precious metal nanoparticles were prepared by adopting a known literature procedure.⁵¹ Briefly, 14 mg of conditioned catalyst powder were ultrasonically dispersed in 2 ml of isopropanol, 3 ml of Millipore water, and $20 \mu\text{l}$ of 5 wt\% Nafion solution (Sigma-Aldrich). For characterization, $10 \mu\text{l}$ of the dispersed catalyst was drop-casted onto a polished glassy carbon electrode and allowed to dry in room air. To capture both ORR and OER activities in one linear sweep, characterization was performed between 0.05 V and 1.7 V for Ru/C , 1.9 V for $\alpha\text{-Mn}_2\text{O}_3$, and 2.2 V for Pt/C . Different anodic potentials were used in different catalytic systems in order to reach an OER current of $10\text{--}20 \text{ mA cm}^{-2}$ in each case; the highest value of 2.2 V used in Pt/C system was not applied to all other catalysts to mitigate carbon oxidation at high anodic potentials. Although the nanoparticles are prepared as metals, at high anodic potentials relevant to OER, the surface of the nanoparticles is converted to a metal oxide. Consequently, while the ORR is observed on metal or on partially oxidized metal surfaces, the OER is observed on the electrochemically formed metal oxide surfaces.

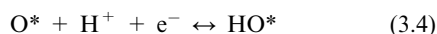
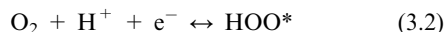
3. The oxygen reduction and oxygen evolution reactions

In an acid environment the ORR and the OER can be written as:

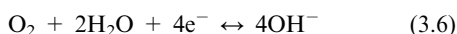


We consider two possible ORR/OER reaction mechanisms: an associative mechanism that involves a HOO^* species, where $*$ represents the active site on the metal surface, and a direct O_2 dissociation/recombination mechanism.

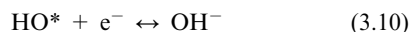
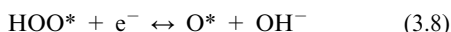
In acid, the associative mechanism goes through the following elementary steps (the ORR proceeds from top to bottom, eqn (3.2) \rightarrow eqn (3.5), where the OER proceeds from bottom to top, eqn (3.5) \rightarrow eqn (3.2):



In an alkaline electrolyte, H_2O rather than H_3O^+ may act as the proton donor, resulting in the overall ORR and OER equation:



The analogous associative mechanism in base is as follows:



Notice that the surface intermediates (HOO^* , O^* , HO^*) are the same in both environments and that they all contain at least one oxygen atom. It is through this oxygen that the intermediates bind to a Mn ion at the surface.

The mechanism *via* direct O_2 dissociation/recombination mechanism consists of the following elementary steps (for simplicity, only the steps in an acid environment are shown):



The ORR and OER mechanisms considered in this study neglect the effect of the electric field in the double layer and do not treat barriers which may depend on whether the proton donor is H_2O or H_3O^+ . Thus, at a fixed potential on the RHE scale, there is no difference in the free energy of the ORR/OER intermediates calculated in acid *versus* in base for the following reasons: (1) all reactions involve the same intermediates and the same number of protons and electrons and (2) a_{H^+} and a_{OH^-} are directly related by means of a pH/pOH scale since water is in equilibrium with H^+ and OH^- .³⁸ As such, we will use the equations derived for the acid solution and apply them to a basic environment to be commensurate with the

experimental data in the base presented herein. Although this method cannot accurately model absolute kinetic rates, the consistent set of assumptions will allow for direct comparison of relative trends in activity. Despite the points made above, we note that for a number of catalyst systems the ORR activity has been found experimentally to be a function of pH. This could arise for a number of reasons, for instance the possibility of an O_2^- reaction pathway in which the step producing O_2^- does not involve binding to the catalyst surface.⁵⁸ Nevertheless, for the most active catalysts like Pt and Ru, the ORR/OER overpotentials are not particularly sensitive to pH and do not proceed through an O_2^- reaction pathway.

4. Results

4.1. Electrochemical characterization

Fig. 2 shows experimental results from our electrochemical characterization of a nanostructured $\alpha\text{-Mn}_2\text{O}_3$ electrode performed in nitrogen and oxygen saturated 0.1 M KOH. Three different data sets are presented in the figure: (1) a base CV in a nitrogen-saturated environment, (2) a CV in an oxygen-saturated environment of the same potential window, and (3) a linear sweep voltammogram (LSV) in a wide potential window in an oxygen-saturated solution. The base CV performed in the nitrogen-saturated environment was used to identify oxidation/reduction features on the nanostructured $\alpha\text{-Mn}_2\text{O}_3$ surface. As seen in the inset of the figure, two oxidation features are observed in the anodic sweep – one between 0.5 and 0.8 V and another between 0.8 and 1.0 V. These features likely correspond to the oxidation of Mn_3O_4 to Mn_2O_3 and Mn_2O_3 to MnO_2 , consistent with the thermodynamic standard potentials for these processes, which are 0.69 V and 1.01 V, respectively.¹³ The reductive feature occurring between 0.90 and 0.65 V in the cathodic sweep of the N_2 -saturated CV pertains to the discharge reaction of MnO_2 to Mn_2O_3 , as assigned in the literature.⁵⁹

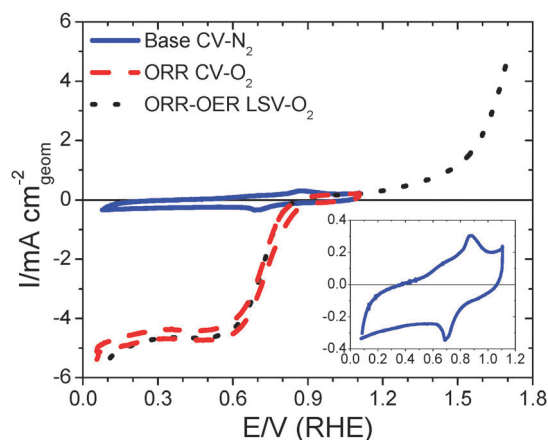


Fig. 2 Electrochemical characterization of an $\alpha\text{-Mn}_2\text{O}_3$ nanostructured thin film. Direct comparison of a base CV in nitrogen (also shown in the inset), a LSV in oxygen. Later in this paper the DFT-produced surface Pourbaix diagram of Fig. 6 shows that the relevant surface for the ORR is Mn_2O_3 and the relevant surface for the OER is MnO_2 .

The CV in the oxygen-saturated environment was used to identify the onset potential for the ORR. The catalyst first draws ORR current at approximately 0.83 V in the cathodic direction (0.80 V in the anodic direction) and reaches a diffusion limited current at 0.60 V. The onset potential of 0.83 V corresponds to an overpotential of 0.4 V, which indicates a highly active non-precious metal ORR catalyst. The experimental LSV reveals that the onset potential for the OER occurs at 1.5 V, which corresponds to an overpotential of 0.27 V and provides evidence of high catalytic activity for the OER. The location of the second oxidation feature between 0.8 V and 1.0 V suggests that during the anodic sweep, the catalyst changes its oxidation state in the potential region between ORR and OER activity. Additionally, since the ORR region is located at the end of the reduction feature seen in the cathodic sweep of the base CV (0.90 V to 0.65 V) and overlaps with an oxidation feature in the anodic sweep of the base CV (0.50 V to 0.80 V), the active surface may undergo changes at different potentials of ORR activity. Spectroscopic methods have been used to study oxidation state changes in MnO_x , however specific identification of the surface phases has remained elusive.³⁵ To identify these phases, we employ theory.

4.2. DFT studies of stable surface structures of MnO_x as a function of pH, applied potential, and starting bulk material

We aim to understand how MnO_x bulk and surface structures change across the pH-potential window, and how these changes impact ORR and OER activity. To do so, we first investigate the relative stability of different adsorbate surface structures for each of three different bulk oxide phases: (a) $\text{Mn}_3\text{O}_4(001)$, (b) $\text{Mn}_2\text{O}_3(110)$ and (c) $\text{MnO}_2(110)$. The MnO_x phase, crystal structure, and the surface adsorbates present during reaction conditions (pH and applied potential) will likely depend on how the material was synthesized in the first place, *e.g.* starting MnO_x crystal structure, nanoparticle size,⁶⁰ *etc.* Here we present a thermodynamic analysis for all possible bulk and surface structures. Though only one combination of a bulk and surface structure can be the *most* thermodynamically stable at a given pH, temperature, and applied potential, it is possible that other structures might be present due to kinetic control, and thus those structures could also contribute to OER and ORR activities.¹³

The calculated free energies for all possible surface adsorbate structures on each of the three bulk structures (Mn_3O_4 , Mn_2O_3 , and MnO_2) are plotted *versus* potential at pH = 0, shown in Fig. S1 in the ESI.† The structure with the lowest free energy at a given potential determines the most likely surface structure as it is the most thermodynamically stable. Fig. 3 then incorporates the effect of pH to produce three surface Pourbaix diagrams in which the most stable surface for each bulk oxide is constructed as a function of pH and the electrode potential *vs.* SHE (U_{SHE}). Later in Section 5, we ultimately combine this information along with thermodynamic data for the bulk oxide phases in order to construct a single General Surface Pourbaix diagram that allows for phase changes both at the surface as well as deeper within the bulk of the near-surface region. We first discuss details of the surface changes for each of the bulk MnO_x phases, as shown in Fig. 3.

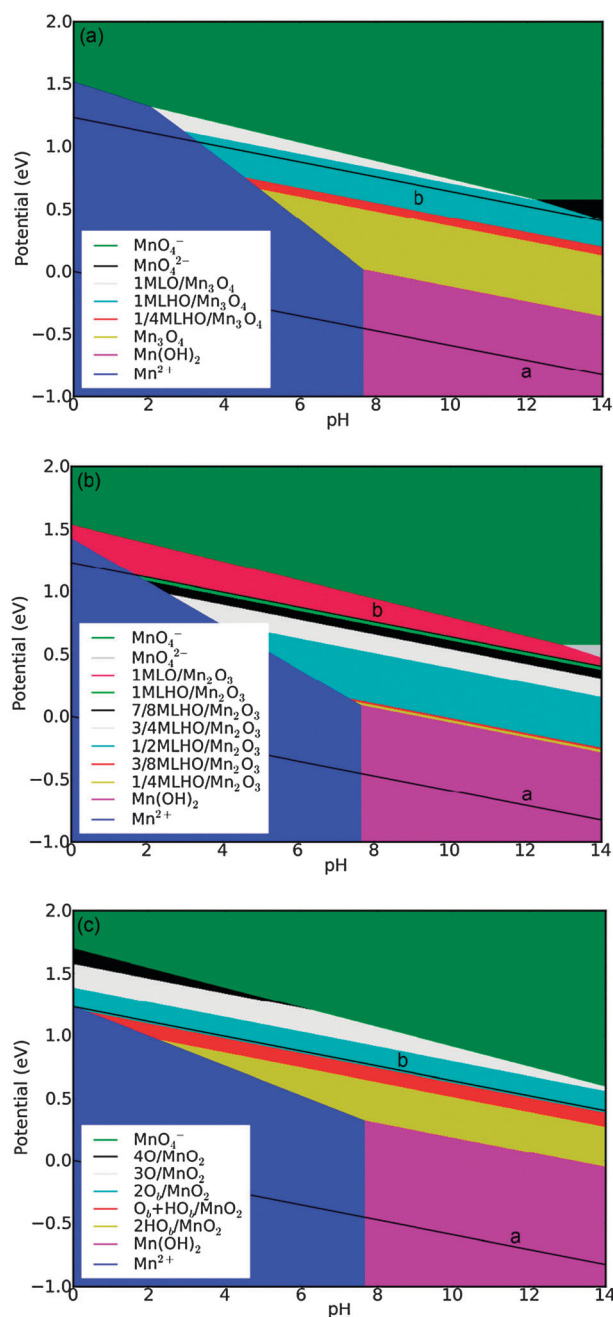


Fig. 3 Surface Pourbaix diagram on (a) $\text{Mn}_3\text{O}_4(001)$, (b) $\text{Mn}_2\text{O}_3(110)$, and (c) $\text{MnO}_2(110)$. Lines a and b represent the reversible hydrogen electrode (RHE) line and the $\text{O}_2/\text{H}_2\text{O}$ equilibrium line. The notation “b” within the Fig. 3(c) legend represents the adsorbates at the bridge sites and coordinated unsaturated sites.

Fig. 3 shows that at low potentials in acidic solutions, dissolution to Mn^{2+} is spontaneous for all MnO_x bulk phases. In alkaline solutions this process is suppressed, and instability is not as problematic as it is in acidic solutions. In both types of electrolytes, corrosion is most severe at potentials higher than 1.46 V (RHE) where the MnO_x can be oxidized and dissolved into MnO_4^- . We thus focus our discussion on the alkaline environment and within that region identify the most stable surface structures as a function of potential on (a) Mn_3O_4 , (b) Mn_2O_3 , and (c) MnO_2 . Note that in Fig. 3

the potential *versus* RHE at any pH can be read off as the vertical distance from line 'a' to the region of interest.

(a) $\text{Mn}_3\text{O}_4(001)$, Fig. 3(a): for the case of $\text{Mn}_3\text{O}_4(001)$, at low potentials ($0.46 \text{ V} < U_{\text{RHE}} < 0.95 \text{ V}$) the clean surface (*i.e.* no adsorbates) is the most stable surface structure. As the potential increases ($0.95 < U_{\text{RHE}} < 1.29 \text{ V}$), water dissociation begins, leading to the presence of HO^* with increasing coverage, *e.g.* 1/4 ML $\text{HO}/\text{Mn}_3\text{O}_4$ and 1 ML $\text{HO}/\text{Mn}_3\text{O}_4$. At potentials $U_{\text{RHE}} > 1.29 \text{ V}$ the adsorbed hydroxyls are oxidized further to O^* to form 1 ML $\text{O}/\text{Mn}_3\text{O}_4$.

(b) $\text{Mn}_2\text{O}_3(110)$, Fig. 3(b): for $\text{Mn}_2\text{O}_3(110)$, water will dissociate to HO^* at potentials $U_{\text{RHE}} > 0.53 \text{ V}$, with HO^* coverage increasing from 1/4-1 ML $\text{HO}/\text{Mn}_2\text{O}_3$ all the way to 1 ML $\text{HO}/\text{Mn}_2\text{O}_3$ by $U_{\text{RHE}} = 1.23 \text{ V}$. At this point, the hydroxyls are oxidized further to produce 1 ML $\text{O}/\text{Mn}_2\text{O}_3$.

(c) $\text{MnO}_2(110)$, Fig. 3(c): at low potentials ($0.78 \text{ V} < U_{\text{RHE}} < 1.1 \text{ V}$), the surface Pourbaix diagram of $\text{MnO}_2(110)$ shows that the bridge sites of $\text{MnO}_2(110)$ are occupied by HO^* ($2\text{OH}_\text{b}/\text{MnO}_2$). The bridge HO^* then gradually dissociates into O^* within the potential region of $1.1 \text{ V} < U_{\text{RHE}} < 1.38 \text{ V}$ ($\text{O}_\text{b} + \text{OH}_\text{b}/\text{MnO}_2$ and $2\text{O}_\text{b}/\text{MnO}_2$). At higher potentials O^* adsorbs at the coordinated-unsaturated sites to form $3\text{O}/\text{MnO}_2$ and $4\text{O}/\text{MnO}_2$.

4.3. Activity of stable MnO_x surface structures for the OER/ORR

Having identified the most thermodynamically stable surface structures as a function of pH and potential for each of the bulk phases of MnO_x , we now look to identify which of those surfaces are likely to be present during OER/ORR operating conditions. To accomplish this goal, we first use ORR/OER free energy diagrams generated by DFT to calculate the theoretical overpotentials for OER/ORR on all the relevant MnO_x surfaces (for more details see Fig. S2 and S3 in ESI†). The “theoretical overpotential” to which we are referring is the overpotential beyond which all reaction steps become thermodynamically downhill. The “theoretical overpotential” is related to, but not identical to, the “onset” potential that is often used as a figure of merit in experimental LSVs. Previously described kinetic models of electrocatalytic reactions show that the experimental “onset” potential is expected to occur approximately 0.15 V prior to the “theoretical overpotential.”⁴² Our calculations of the reaction energetics for the OER/ORR are not shown for every possible surface configuration in Fig. 3, but rather only for the ‘self-consistent’ catalytic surfaces; that is, the surfaces that are thermodynamically stable, according to the Pourbaix diagrams of Fig. 3, at the overpotential at which catalyst is operating.

At the high potentials required to drive the OER, the self-consistent surfaces for each of the three MnO_x bulk phases are quite similar – they are all completely covered by oxygen. This is in agreement with our previous work investigating the OER on rutile oxide surfaces. Since the oxide surfaces are covered with oxygen at OER relevant potentials, no active sites are available for water adsorption,³⁸ and thus the effect of water and its interactions with adsorbed reaction intermediates can be neglected. This simplifies the analysis of OER reaction energetics substantially.

At ORR potentials, however, the effect of water cannot be neglected as there are available sites for water to adsorb and potentially dissociate into HO^* and O^* . This leads to considerably different MnO_x adsorbate surface structures for each of the three bulk structures, namely clean $\text{Mn}_3\text{O}_4(001)$, 1/2 ML HO^* covered $\text{Mn}_2\text{O}_3(110)$ and $\text{MnO}_2(110)$ with HO^* at bridge sites as spectators. Notice that for all of these surfaces, there are empty sites where water can adsorb and impact the adsorption energies of ORR intermediates, particularly with HO^* and HOO^* as these adsorbates can form H bonds with adjacent water molecules. Therefore, the effect of water is included in the free energy diagram for intermediates involved in the ORR.

Detailed studies on metals⁶¹ have shown that water stabilizes surrounding HO^* and HOO^* species by -0.3 eV . In our preliminary studies of this effect for metal oxide surfaces, we investigated a single neighboring water molecule interacting with HO^* and HOO^* adsorption on an $\text{MnO}_2(110)$ surface. We obtained similar stabilization effects of -0.5 eV and -0.35 eV , respectively. For the purposes of this work, we choose to use -0.3 eV for the stabilization effect of water on both HO^* and HOO^* intermediates and note that more detailed studies of the effects of water at metal oxide interfaces will be considered in future studies.

We note that in this work we identify surface structures based solely on static equilibrium considerations. Under reaction conditions the local coverage of reaction intermediates is in a very dynamic state, and these dynamics could very well play a role on the reaction chemistry. For low rates of reaction, however (*i.e.* near the experimental ‘onset’ potential, which occurs before the theoretical overpotential), the surface Pourbaix diagram is a good model for determining the self-consistent surface.

Free energy diagrams constructed for the self-consistent surfaces, shown in Fig. 4, provide insight into the mechanistic pathways involved in oxygen reduction and oxygen evolution. They also point out the source of reaction overpotentials for each surface, exactly the kind of information needed to facilitate the development of improved catalysts.

The free energy calculations for the OER indicate that for O^* covered $\text{Mn}_3\text{O}_4(001)$ and O^* covered $\text{Mn}_2\text{O}_3(110)$, the associative pathway is energetically favorable compared to the direct mechanism. For the O^* covered $\text{MnO}_2(110)$ surface, however, the direct pathway is slightly favored. Previous studies have shown that the OER activity of metal oxides follow a ‘volcano’ relationship based on scaling relations that correlate binding energies for the different reaction intermediates.⁶² The O^* covered $\text{MnO}_2(110)$ surface is close to the top of the volcano where the intermediates have a better compromise in interaction strength, which results in a more flexible reaction mechanism. In this case, the direct mechanism by recombination of oxygen atoms has a slightly lower free energy than associative mechanism by only 0.08 eV , as described in the Fig. S3(b) (ESI†).

To gain more information about the sources of overpotential on the self-consistent MnO_x surfaces, we compared those free energy diagrams with that of an ideal oxygen evolution/reduction catalyst, shown in Fig. 4(a). The ideal catalyst is defined by a free energy reaction diagram in which

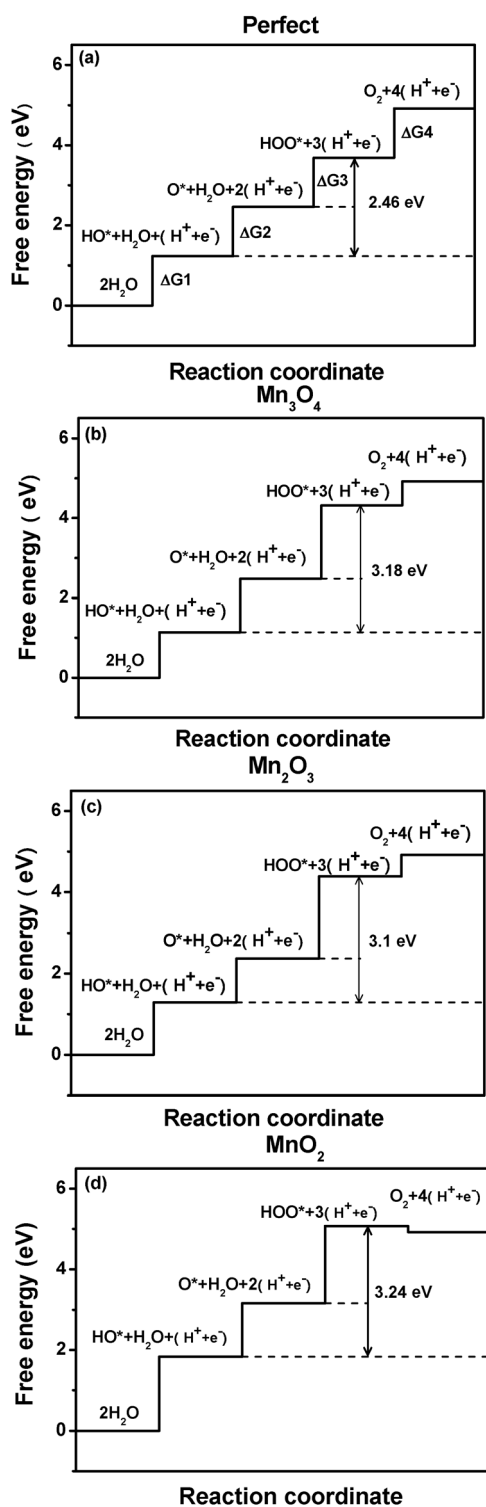


Fig. 4 Free-energy diagram for the oxygen evolution reaction on (a) the perfect catalyst, and O covered (b) $\text{Mn}_3\text{O}_4(001)$, (c) $\text{Mn}_2\text{O}_3(110)$ and (d) $\text{MnO}_2(110)$ at $U = 0$, $\text{pH} = 0$ and $T = 298$ K. $\Delta G_{\text{HOO}^*} - \Delta G_{\text{HO}^*}$ (vertical solid lines) values of the three manganese oxides in (b), (c), and (d), are close to 3.2 eV, the average value found on a wide range of metals and oxides as shown in our recent paper in ref 56. The optimum value on the perfect catalyst is 2.46 eV.

the four charge transfer steps have identical reaction free energies of $1.23 \text{ eV} = 4.92 \text{ eV}/4$ for an electrode held at $U_{\text{SHE}} = 0$.

If one is able to tune the binding energy of each intermediate on a surface to achieve this optimal situation, that catalyst surface would approach the activity of an ideal oxygen electrode. However, as illustrated in recent work,^{62,63} there is a universal scaling relationship on a wide range of metals and oxides that governs the binding energy of the HOO^* intermediate with respect to HO^* , resulting in an approximately constant difference between the two energy levels ($\Delta G_{\text{HOO}^*} - \Delta G_{\text{HO}^*} \approx 3.2 \text{ eV}$). This is far off of an optimal catalyst which would exhibit an energy difference of 2.46 eV ($2e \times 1.23\text{V}$) between those two particular energy levels. Thus, the ‘universal’ 3.2 eV energy difference between HOO^* and HO^* levels can be used to define the lowest possible “theoretical overpotential” for the OER and the ORR [$(3.2 \text{ eV} - 2.46 \text{ eV})/2e \approx 0.37 \text{ V}$] on a wide variety of materials. The scaling relationship between HOO^* and HO^* holds for MnO_x just as well, as shown in Fig. 4(b), (c) and (d), with values of 3.18 eV, 3.1 eV and 3.12 eV. The slight deviation of $\Delta G_{\text{HOO}^*} - \Delta G_{\text{HO}^*}$ from 3.2 eV can be attributed to adsorbate coverage effects.

Indeed, the scaling relationship between the HOO^* and HO^* binding energies explains one major source of reaction overpotential, however additional sources of overpotential can also arise from sub-optimal O^* binding. It has been previously shown that the potential-determining step for the OER is either the second water dissociation step eqn (3.3) or the HO^* oxidation step eqn (3.4).³⁸ Both steps involve O^* and either HOO^* or HO^* ; as the latter two species scale linearly with one another, the expression $(\Delta G_{\text{O}^*} - \Delta G_{\text{HO}^*})$ contains information regarding the binding energies for all three species and is introduced as the universal descriptor of oxygen evolution activities.

We can see from Fig. 4(b) and (c) that for the OER, the O^* covered $\text{Mn}_3\text{O}_4(001)$ and $\text{Mn}_2\text{O}_3(110)$ have the same potential-determining step, the second water dissociation step eqn (3.3) in which the third (of four) H^+ and e^- are transferred. The O^* covered $\text{Mn}_3\text{O}_4(001)$ surface exhibits a lower “theoretical overpotential” than the O^* covered $\text{Mn}_2\text{O}_3(110)$ surface, 0.6 V vs. 0.79 V. This originates from the placement of the O^* energy level with respect to the energy levels of the intermediates below (HO^*) and above (HOO^*) it; closer to half-way is better in order to prevent large uphill reaction steps. For the O^* covered MnO_2 surface, the second water dissociation eqn (3.3) is also the potential-determining step, according to the associative mechanism (see Fig. 4(d)), leading to a “theoretical overpotential” of 0.6 V.

For the ORR, the same scaling relationship holds between HOO^* and HO^* . Thus, much like the OER, one part of the ORR overpotential originates from this correlation while the other part arises from sub-optimal O^* binding. The free energy diagrams of the intermediates for the ORR on the self-consistent MnO_x surfaces are shown in Fig. 5. Our previous studies have shown that the potential-determining ORR step is either the formation of HOO^* eqn (3.2) or the reduction of HO^* eqn (3.5).³⁸ As HO^* and HOO^* scale linearly with one another, ΔG_{HO^*} can be introduced as a universal descriptor of oxygen reduction activities. We can see that all three self-consistent MnO_x surfaces – clean $\text{Mn}_3\text{O}_4(001)$, 1/2 ML HO^* covered $\text{Mn}_2\text{O}_3(110)$ and 1/2 ML HO^* (bridge) $\text{MnO}_2(110)$ – are active for the ORR. The potential-determining step is HO^*

reduction for the first two oxides while for MnO_2 it is HOO^* formation. Calculated “theoretical overpotentials” are approximately 0.55–0.57 V for all cases.

As mentioned above, water can stabilize ORR intermediates during reaction and, as a result, changes in water coverage and the number of hydrogen bonds could influence the calculated overpotentials. A more detailed study of water adsorption and its effects on stabilizing reaction intermediates would provide a more accurate estimate of “theoretical overpotentials.”

5. Discussion

The Pourbaix diagrams generated in Fig. 3 describe changes in adsorbate surface structure as a function of pH and potential for three different MnO_x bulk structures. One question that arises is what if the bulk structure of the catalyst could change with respect to pH and potential? In Fig. 6, we present a general MnO_x Pourbaix diagram that accounts for phase transitions in both the bulk (*e.g.* in the near-surface region) and at the very surface of the catalyst. As seen in Fig. 6, from $0.46 \text{ V} < U_{\text{RHE}} < 0.69 \text{ V}$, the most stable MnO_x bulk/surface is a clean (adsorbate-free) $\text{Mn}_3\text{O}_4(001)$ surface. From $0.69 \text{ V} < U_{\text{RHE}} < 0.98 \text{ V}$, the material is oxidized into $1/2 \text{ ML HO}^*$ covered $\text{Mn}_2\text{O}_3(110)$, assuming no kinetic difficulties. From $0.98 \text{ V} < U_{\text{RHE}} < 1.01 \text{ V}$ the $\text{Mn}_2\text{O}_3(110)$ surface remains, however HO^* coverage increases to $3/4 \text{ ML}$. Between $1.01 \text{ V} < U_{\text{RHE}} < 1.21 \text{ V}$, the bulk is oxidized from Mn_2O_3 to $\text{MnO}_2(110)$ and at the surface, bridge sites are covered with HO^* . As the potential increases above 1.21 V , the surface is further oxidized until the surface is completely covered by O^* . At even higher potentials the MnO_4^- dissolution becomes thermodynamically favourable at any pH.

In combination with the “theoretical overpotentials” for the ORR and the OER on relevant surface structures of $\text{Mn}_3\text{O}_4(001)$, $\text{Mn}_2\text{O}_3(110)$, $\text{MnO}_2(110)$ as described in Fig. 4 and Fig. 5, we can use the DFT-calculated general MnO_x Pourbaix diagram to identify the active surfaces during operating conditions. We find that for the ORR, the active surface in the onset region is a $1/2 \text{ ML HO}^*$ covered $\text{Mn}_2\text{O}_3(110)$, while for the OER, the active surface is O^* covered $\text{MnO}_2(110)$. The predicted change in the oxidation state from Mn(III) in Mn_2O_3 to Mn(IV) in MnO_2 in the potential region between the ORR and the OER is supported by the oxidation feature between 0.8 V and 1.0 V seen in the anodic sweep of the base CV (Fig. 2).

“Theoretical onset potentials” for the ORR and OER were calculated for these two surfaces by subtracting 0.15 V from the “theoretical overpotentials” based on the kinetic models described earlier, resulting in calculated values of 0.40 V and 0.45 V , respectively. These values are in good agreement with the experimentally observed onset potentials of 0.4 for the ORR and 0.27 for the OER measured on the nanostructured $\alpha\text{-Mn}_2\text{O}_3$ electrocatalyst.

To visually relate theoretical predictions of ORR/OER activities to experimental results, we used the Sabatier model⁴² to create theoretical LSVs for the ORR and the OER (Fig. 7). Constructing the theoretical LSVs could only be possible by having first identified the most thermodynamically stable bulk and surface structures present during reaction conditions.

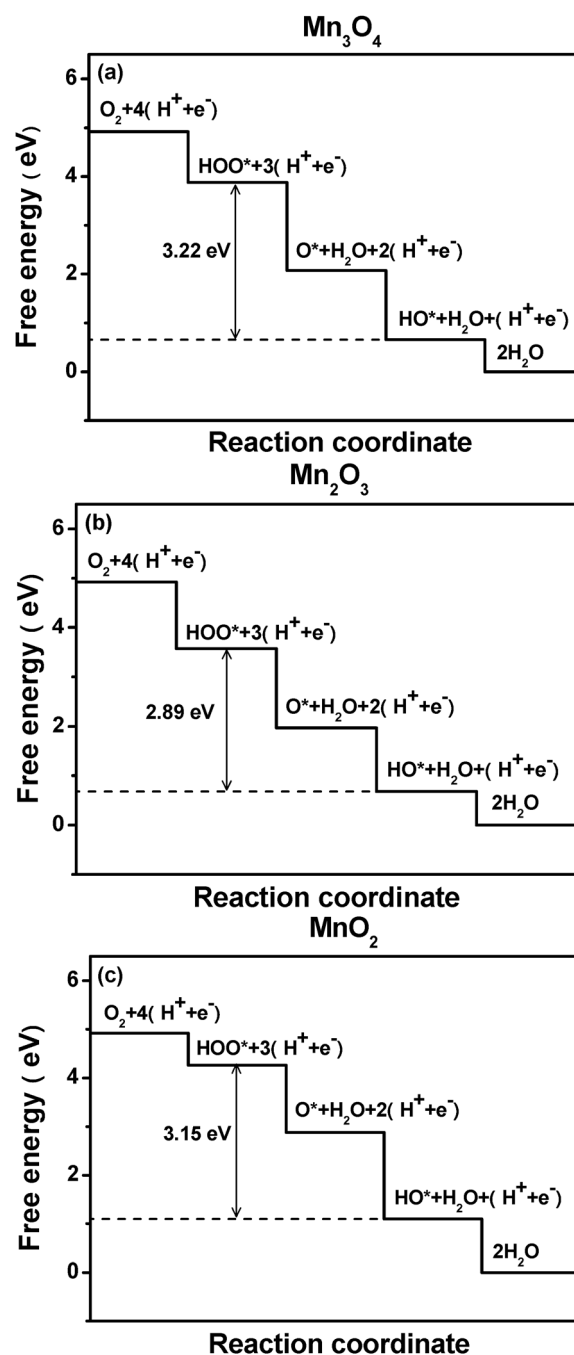


Fig. 5 Free-energy diagram for oxygen reduction on (a) $\text{Mn}_3\text{O}_4(001)$, (b) $1/2 \text{ ML HO}^*$ covered $\text{Mn}_2\text{O}_3(110)$ and (c) $\text{MnO}_2(110)$ with HO^* at bridge sites as spectators at $U = 0$, $\text{pH} = 0$ and $T = 298 \text{ K}$.

In producing these theoretical LSVs, diffusion limitations for the ORR are included by invoking the Koutecky–Levich equation for a rotating disk at 1600 RPM.⁶⁴ Fig. 7(a) shows theoretical LSVs for the self-consistent surface structures pertaining to bulk $\text{Mn}_3\text{O}_4(001)$, $\text{Mn}_2\text{O}_3(110)$ and $\text{MnO}_2(110)$, constructed as if no changes in bulk MnO_x stoichiometry were induced by the electrochemical potential. In other words, the bulk structure was fixed throughout the entire potential window – only the surface was allowed to change as shown in Fig. 3. Fig. 7(a) thus reveals the intrinsic catalytic activities of bulk $\text{Mn}_3\text{O}_4(001)$, $\text{Mn}_2\text{O}_3(110)$ and $\text{MnO}_2(110)$ structures. All three bulk MnO_x structures are

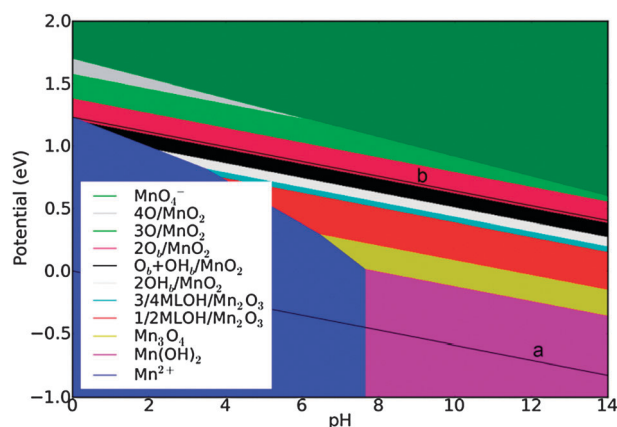


Fig. 6 General surface Pourbaix diagram for MnO_x catalysts. The oxidation state of the surface and the ORR and OER potential are constant *versus* the reversible hydrogen electrode (RHE). Lines a and b represent the RHE line and the $\text{O}_2/\text{H}_2\text{O}$ equilibrium line.

shown to be highly active ORR catalysts. However, for the OER only O^* covered $\text{MnO}_2(110)$ and O^* covered $\text{Mn}_3\text{O}_4(001)$ are highly active.

Fig. 7(b) shows a theoretical LSV in which both the bulk structure and the surface structure are allowed to change with applied potential. Fig. 7(b) is most relevant for MnO_x catalysts with negligible kinetic barriers to phase changes in the near-surface region, thus allowing both the bulk and the surface to reach their thermodynamically stable structures. For such a catalyst, the ORR has two relevant active surfaces. At the ORR onset potential of 0.83 V, the active surface is a 1/2 ML HO^* covered $\text{Mn}_2\text{O}_3(110)$. However, as the potential decreases below 0.69 V and the current approaches diffusion-limited values, the 1/2 ML HO^* covered $\text{Mn}_2\text{O}_3(110)$ is predicted to be reduced to clean $\text{Mn}_3\text{O}_4(001)$ surface. This DFT-predicted change in the oxidation state of MnO_x is supported by the oxidation feature between 0.5 V and 0.8 V seen in the anodic sweep of the base CV, Fig. 2.

In the OER region of Fig. 7(b), the theoretical OER activity of the self-consistent MnO_x surface is also shown. At the high potentials of the OER, O^* covered MnO_2 is the expected bulk-surface combination. Fig. 7(b) also compares the theoretical LSVs of MnO_x in both the ORR and OER regions to those of self-consistent Ru and Pt, in which phase transitions to RuO_2 and PtO_2 at oxidative potentials were taken into account.¹³ According to theoretical LSVs shown in Fig. 7(b), the predicted activity order for the OER is $\text{RuO}_2 > \text{MnO}_2 > \text{PtO}_2$, and for the ORR is $\text{Pt} > \text{Mn}_2\text{O}_3 > \text{Ru}$. We note that this same model has previously been successful in predicting the trends in ORR activity for metal-alloy catalysts.^{36,39} We now turn our attention to comparing theoretical predictions with experimental measurements for MnO_x , Pt, and Ru catalysts.

Fig. 7(c) shows experimental LSVs for the nanostructured $\alpha\text{-Mn}_2\text{O}_3$, Ru/C and Pt/C. Pt/C demonstrates the best ORR activity, while the oxidized Ru/C demonstrates the best OER activity. The nanostructured $\alpha\text{-Mn}_2\text{O}_3$ shows high activity for both reactions. Under reductive potentials relevant to the ORR, the Mn_2O_3 surface outperforms Ru/C and approaches activity of Pt/C, while under oxidative potentials relevant to the OER, the MnO_2 surface outperforms the oxidized Pt/C

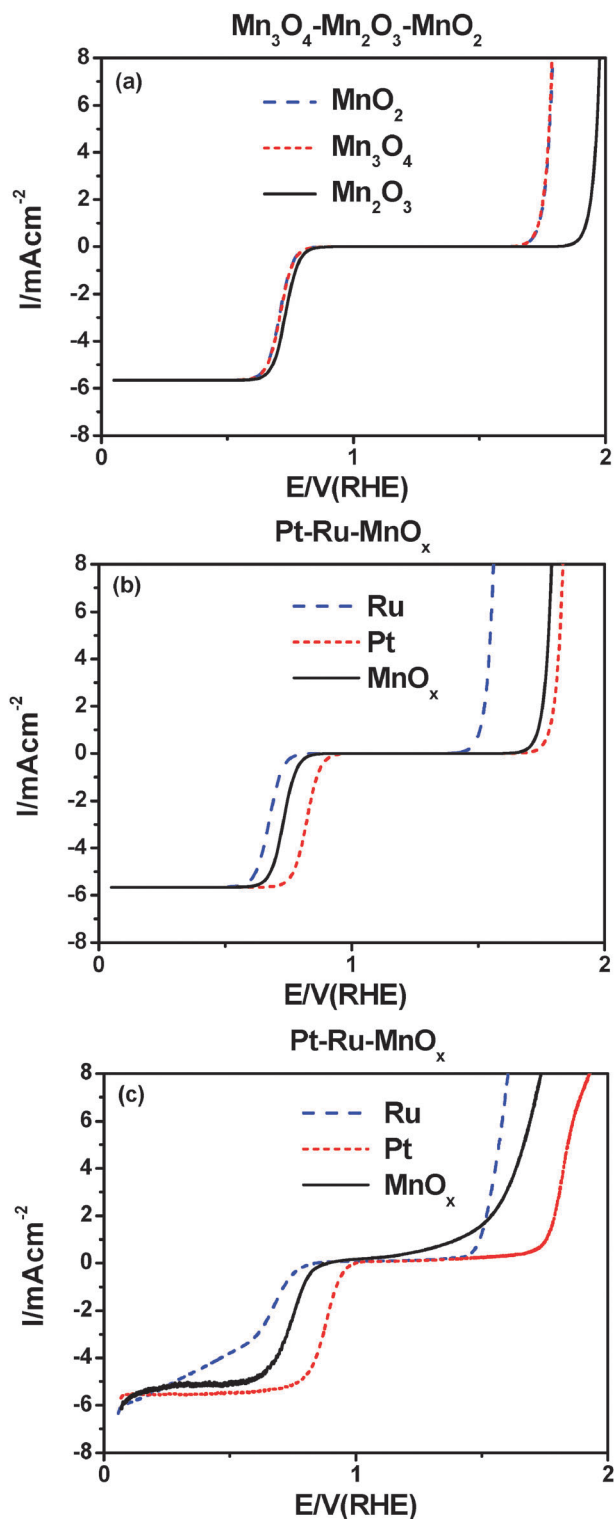


Fig. 7 Calculated current density for (a) Mn_3O_4 , Mn_2O_3 and MnO_2 ; (b) self-consistent curves from DFT calculation for MnO_x , Ru and Pt; (c) experimental curves for MnO_x , Ru and Pt.

and approaches the activity of the oxidized Ru/C. For both the ORR and the OER, the experimental activity trends are identical to those predicted by the DFT models. There is also excellent quantitative agreement between theory and experiment.

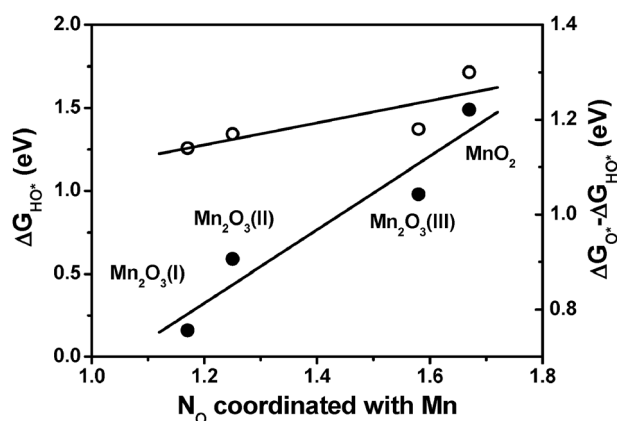


Fig. 8 The free energy of HO* (ΔG_{HO^*} , solid circle) and the free energy difference between O* and HO* ($\Delta G_{\text{O}^*} - \Delta G_{\text{HO}^*}$, open circle) plot against the number of O (N_{O}) coordinated with Mn on $\text{Mn}_2\text{O}_3(110)$ and $\text{MnO}_2(110)$. I, II and III represent three different types of Mn atoms on the $\text{Mn}_2\text{O}_3(110)$ surface respectively.

Only minor discrepancies are observed between the theoretically-predicted and the experimentally-observed onset potentials for MnO_x . One possible source of the discrepancies could be due the assumptions made about the number of oxygen atoms, N_{O} , coordinated to each Mn atom at the MnO_x surface in the DFT calculations. This theoretical study focuses solely on β - MnO_2 amongst the MnO_2 family as this is the most stable of its phases. However, the presence of α - MnO_2 and γ - MnO_2 phases can be expected in experimental MnO_2 electrodes,^{19,21,22,26,28} and the coordination environment of these phases will exhibit different values of N_{O} . Furthermore, the theoretical calculations of the catalyst surface structure as a function of electrochemical potential (Fig. 3) examined the changes in the MnO_x structure only in the top-most layer. During the experiments, however, it is quite possible that complete or incomplete stoichiometric changes could penetrate deeper into the material and impact N_{O} , which can lead to significant variation in electrochemical activity. Some, but not all, of the possibilities are accounted for in Fig. 6, the general Pourbaix diagram. Fig. 8 shows the origin of this particular effect, exhibiting the relationships among (1) the free energy of HO* (ΔG_{HO^*} , descriptor for ORR activity), (2) the free energy difference between O* and HO* ($\Delta G_{\text{O}^*} - \Delta G_{\text{HO}^*}$, descriptor for OER activity), and (3) N_{O} , the number of oxygen atoms coordinated to surface Mn (see ESI for a sample calculation of N_{O}). For the case of Mn_2O_3 surfaces, as the oxygen coordination number increases, ΔG_{HO^*} changes only marginally, while $\Delta G_{\text{O}^*} - \Delta G_{\text{HO}^*}$ changes by 0.7 eV, which means that the catalytic activities of manganese oxides can sometimes, but not always, be sensitive to oxygen coordination at the surface.

The close match between theoretical predictions and experimental results suggests that we have successfully modelled the surface structure of MnO_x catalysts, and in particular how metal oxide surfaces change with pH and applied electrochemical potential. We have also successfully simulated the catalytic activity of those surfaces for the ORR and the OER, having identified the active surface structure as well as the reaction pathways involved. This insight gained from DFT calculations can now be used to improve the design principles

for OER/ORR catalysts. For example, our theoretical calculations have identified that the stabilization of intermediates through hydrogen bonds with water is an important contributor to ORR overpotential on MnO_x catalysts. Therefore, a rational design of more hydrophobic catalyst structures, resulting in a reduced number of water molecules adsorbed on the surface, can lead to a significant improvement in ORR activity of MnO_x catalysts. Our calculations have also demonstrated that an O* covered MnO_2 surface is close to the top of OER volcano. Therefore, to improve the activity of O* covered MnO_2 for OER, it will be necessary to modify the catalyst surface in such a way as to break the scaling relationship between the energies of HOO* and HO* intermediates. Finally, our finding that the number of oxygen atoms coordinated to each Mn atom at the MnO_x surface has a significant impact on the binding energy of reaction intermediates suggests that manipulation of the surface coordination environment, through approaches such as nanostructuring, doping, and alloying, can also lead to improved manganese oxide electrocatalysts for the ORR and the OER.

6. Conclusions

The surface electrochemistry of metal oxide catalysts is complex. Phase changes are prevalent both at the surface and in the near-surface region that depend greatly on pH and applied potential. And the structure of the material, both at the surface and within the bulk, has a significant influence on catalyst activity. In this work, we combine theory and experiment to understand this chemistry for the specific case of MnO_x materials that catalyze the ORR and the OER. The theoretical models developed in this work, however, are more broadly applicable to other metal oxides as well as to other electrocatalytic reactions.

Experimentally, we have shown that a nanostructured α - Mn_2O_3 is an excellent bi-functional catalyst for the ORR and the OER, and that the catalyst likely undergoes phase changes at the surface as a function of applied potential, in particular at ORR potentials and in the potential window between the ORR and the OER. In an effort to understand surface changes under reaction conditions, as well as how they impact catalytic activity and reaction pathways for both reactions, we developed theoretical models using density functional theory (DFT). DFT calculations were employed to construct surface Pourbaix diagrams for MnO_x and then to identify “theoretical overpotentials” for the surfaces present during reaction conditions across the pH and potential window. Our calculations reveal that the active surfaces for the ORR and the OER are 1/2 ML HO* covered Mn_2O_3 and O* covered MnO_2 , respectively. As shown in Fig. 7(b), this phase transition between the two operating conditions is beneficial in that MnO_2 is a better catalytic surface for the OER than Mn_2O_3 . Thus an active catalyst phase is formed under each of the two reaction conditions.

The calculations also suggest mechanistic pathways for the ORR and the OER on the relevant surface structures: the ORR proceeds by the associative pathway, while for the OER, the direct pathway is favored slightly. With these calculations we were able to construct theoretical LSVs for MnO_x which

make predictions on catalytic activity for the ORR and the OER. The theoretical LSVs agree well with the experimental LSVs measured on the active nanostructured MnO_x bi-functional catalyst; the close match between theory and experiment suggests that the theoretical model is accurate and robust.

By combining first-principles theoretical analysis and experimental methods, atomic-level insight into the catalyst chemistry can be achieved. This allows one to determine principles for improving catalyst design. For the ORR, our DFT model predicts that decreasing the surface's affinity for water adsorption should significantly increase catalytic activity, as it is desirable to destabilize the reaction intermediates HOO^* and HO^* . For the OER, our calculations show that to improve the activity of MnO_x , it is necessary to design a surface structure that can break the scaling relationship between the energies of HOO^* and HO^* intermediates. If future ORR and OER catalysts are developed with these design principles in mind, superior activity for both reactions can be achieved.

Acknowledgements

We gratefully acknowledge funding from the Danish Strategic Research Council's HyCycle program, the Danish Council for Technology and Innovation's FTP program. This research was supported in part by the European Commission (Marie Curie Research Training Network MRTN-CT-2006-032474), by the Danish Council for Strategic Research via SERC project through grant no. 2104-06-011 and by the Catalysis for Sustainable Energy (CASE) initiative. This work was partially supported by the IMI Program of the National Science Foundation under Award No. DMR 0843934. YG, TFJ, and JKN were supported by the Center on Nanostructuring for Efficient Energy Conversion (CNEEC) at Stanford University, an Energy Frontier Research Center funded by the U.S. Department of Energy, Office of Science, Office of Basic Energy Sciences under Award Number DE-SC0001060.

Notes and References

- R. Forgie, G. Bugosh, K. C. Neyerlin, Z. C. Liu and P. Strasser, *Electrochem. Solid-State Lett.*, 2010, **13**, D36–D39.
- H. Dau, C. Limberg, T. Reier, M. Risch, S. Roggan and P. Strasser, *ChemCatChem*, 2010, **2**, 724–761.
- M. W. Kanan and D. G. Nocera, *Science*, 2008, **321**, 1072–1075.
- K. Macounova, M. Makarova and P. Krtil, *Electrochem. Commun.*, 2009, **11**, 1865–1868.
- M. V. Makarova, J. Jirkovsky, M. Klementova, I. Jirka, K. Macounova and P. Krtil, *Electrochim. Acta*, 2008, **53**, 2656–2664.
- G. Y. Chen, S. R. Bare and T. E. Mallouk, *J. Electrochem. Soc.*, 2002, **149**, A1092–A1099.
- N. S. Lewis and D. G. Nocera, *Proc. Natl. Acad. Sci. U. S. A.*, 2006, **103**, 15729–15735.
- S. Chretien and H. Metiu, *J. Chem. Phys.*, 2008, **129**, 074705, DOI: 10.1063/1.2956506.
- P. Mani, R. Srivastava and P. Strasser, *J. Phys. Chem. C*, 2008, **112**, 2770–2778.
- T. Ioroi, N. Kitazawa, K. Yasuda, Y. Yamamoto and H. Takenaka, *J. Appl. Electrochem.*, 2001, **31**, 1179–1183.
- H. Liu, B. L. Yi, M. Hou, J. F. Wu, Z. J. Hou and H. M. Zhang, *Electrochem. Solid-State Lett.*, 2004, **7**, A56–A59.
- L. L. Swette, A. B. Laconti and S. A. McCatty, *J. Power Sources*, 1994, **47**, 343–351.
- M. Pourbaix, *Atlas of Electrochemical Equilibria in Aqueous Solutions*, Pergamon Press, New York, 1966.
- K. N. Ferreira, T. M. Iversen, K. Maghlaoui, J. Barber and S. Iwata, *Science*, 2004, **303**, 1831–1838.
- B. Loll, J. Kern, W. Saenger, A. Zouni and J. Biesiadka, *Nature*, 2005, **438**, 1040–1044.
- J. Rossmeisl, K. Dimitrievski, P. Siegbahn and J. K. Nørskov, *J. Phys. Chem. C*, 2007, **111**, 18821–18823.
- P. E. M. Siegbahn and M. Lundberg, *J. Inorg. Biochem.*, 2006, **100**, 1035–1040.
- M. L. Calegario, F. H. B. Lima and E. A. Ticianelli, *J. Power Sources*, 2006, **158**, 735–739.
- Y. L. Cao, H. X. Yang, X. P. Ai and L. F. Xiao, *J. Electroanal. Chem.*, 2003, **557**, 127–134.
- F. Y. Cheng, Y. Su, J. Liang, Z. L. Tao and J. Chen, *Chem. Mater.*, 2010, **22**, 898–905.
- M. I. A. M. S. El-Deab, A. M. Mohammad and T. Ohsaka, *Electrochem. Commun.*, 2007, **9**, 2082–2087.
- M. S. El-Deab and T. Ohsaka, *J. Electrochem. Soc.*, 2008, **155**, D14–D21.
- F. Jiao and H. Frei, *Chem. Commun.*, 2010, **46**, 2920–2922.
- F. H. B. Lima, M. L. Calegario and E. A. Ticianelli, *J. Electroanal. Chem.*, 2006, **590**, 152–160.
- F. H. B. Lima, M. L. Calegario and E. A. Ticianelli, *Electrochim. Acta*, 2007, **52**, 3732–3738.
- A. M. Mohammad, M. I. Awad, M. S. El-Deab, T. Okajima and T. Ohsaka, *Electrochim. Acta*, 2008, **53**, 4351–4358.
- I. Roche, E. Chânet, M. Chatenet and J. Vondrak, *J. Phys. Chem. C*, 2007, **111**, 1434–1443.
- L. Q. Mao, T. Sotomura, K. Nakatsu, N. Koshiba, D. Zhang and T. Ohsaka, *J. Electrochem. Soc.*, 2002, **149**, A504–A507.
- L. Q. Mao, D. Zhang, T. Sotomura, K. Nakatsu, N. Koshiba and T. Ohsaka, *Electrochim. Acta*, 2003, **48**, 1015–1021.
- J. S. Yang and J. J. Xu, *Electrochem. Commun.*, 2003, **5**, 306–311.
- Y. Gorlin and T. F. Jaramillo, *J. Am. Chem. Soc.*, 2010, **132**, 13612–13614.
- N. Ramaswamy, R. J. Allen and S. Mukerjee, *J. Phys. Chem. C*, 2011, **115**, 12650–12664.
- N. Sivasankar, W. W. Weare and H. Frei, *J. Am. Chem. Soc.*, 2011, **133**, 12976–12979.
- B. S. Yeo and A. T. Bell, *J. Am. Chem. Soc.*, 2011, **133**, 5587–5593.
- Y. Gorlin and T. F. Jaramillo, *ECS Trans.*, 2011, **41**, 1701–1707.
- J. Greeley, I. E. L. Stephens, A. S. Bondarenko, T. P. Johansson, H. A. Hansen, T. F. Jaramillo, J. Rossmeisl, I. Chorkendorff and J. K. Nørskov, *Nat. Chem.*, 2009, **1**, 552–556.
- J. K. Nørskov, J. Rossmeisl, A. Logadottir, L. Lindqvist, J. R. Kitchin, T. Bligaard and H. Jonsson, *J. Phys. Chem. B*, 2004, **108**, 17886–17892.
- J. Rossmeisl, Z. W. Qu, H. Zhu, G. J. Kroes and J. K. Nørskov, *J. Electroanal. Chem.*, 2007, **607**, 83–89.
- V. Stamenkovic, B. S. Mun, K. J. J. Mayrhofer, P. N. Ross, N. M. Markovic, J. Rossmeisl, J. Greeley and J. K. Nørskov, *Angew. Chem., Int. Ed.*, 2006, **45**, 2897–2901.
- H. A. Hansen, I. C. Man, F. Studt, F. Abild-Pedersen, T. Bligaard and J. Rossmeisl, *Phys. Chem. Chem. Phys.*, 2010, **12**, 283–290.
- H. A. Hansen, J. Rossmeisl and J. K. Nørskov, *Phys. Chem. Chem. Phys.*, 2008, **10**, 3722–3730.
- J. Rossmeisl, G. S. Karlberg, T. Jaramillo and J. K. Nørskov, *Faraday Discuss.*, 2008, **140**, 337–346.
- B. Hammer, L. B. Hansen and J. K. Nørskov, *Phys. Rev. B: Condens. Matter Mater. Phys.*, 1999, **59**, 7413–7421.
- D. Vanderbilt, *Phys. Rev. B: Condens. Matter Mater. Phys.*, 1990, **41**, 7892–7895.
- V. Bayer, C. Franchini and R. Podloucky, *Phys. Rev. B: Condens. Matter Mater. Phys.*, 2007, **75**, 035404, DOI: 10.1103/PhysRevB.75.035404.
- V. Bayer, R. Podloucky and C. Franchini, *Phys. Rev. B: Condens. Matter Mater. Phys.*, 2007, **76**, 165428, DOI: 10.1103/PhysRevB.76.165428.
- A. K. Cheetham and D. A. O. Hope, *Phys. Rev. B: Condens. Matter Mater. Phys.*, 1983, **27**, 6964–6967.
- C. Franchini, V. Bayer, R. Podloucky, J. Paier and G. Kresse, *Phys. Rev. B: Condens. Matter Mater. Phys.*, 2005, **72**, 045132, DOI: 10.1103/PhysRevB.72.045132.

- 49 C. Franchini, R. Podloucky, J. Paier, M. Marsman and G. Kresse, *Phys. Rev. B: Condens. Matter Mater. Phys.*, 2007, **75**, 224120, DOI: 10.1103/PhysRevB.75.224120.
- 50 B. E. F. Fender, A. J. Jacobson and F. A. Wedgwood, *J. Chem. Phys.*, 1968, **48**, 990–995.
- 51 S. Mukherjee, A. K. Pal, S. Bhattacharya and J. Raittila, *Phys. Rev. B: Condens. Matter Mater. Phys.*, 2006, **74**, 104413, DOI: 10.1103/PhysRevB.74.104413.
- 52 D. B. Rogers, R. D. Shannon, A. W. Sleight and J. L. Gillson, *Inorg. Chem.*, 1969, **8**, 841–849.
- 53 W. G. Wyckoff, *Crystal Structures*, Wiley, New York, 1963.
- 54 S. A. Chambers and Y. Liang, *Surf. Sci.*, 1999, **420**, 123–133.
- 55 P. Jones and J. A. Hockey, *Trans. Faraday Soc.*, 1971, **67**, 2679–2685.
- 56 J. Rossmeisl, J. K. Nørskov, C. D. Taylor, M. J. Janik and M. Neurock, *J. Phys. Chem. B*, 2006, **110**, 21833–21839.
- 57 P. W. Atkins, *Phys. Chem.*, Oxford University Press, Oxford, 1998.
- 58 N. Ramaswamy and S. Mukerjee, *J. Phys. Chem. C*, 2011, **115**, 18015–18026.
- 59 A. Kozawa and R. A. Powers, *J. Electrochem. Soc.*, 1966, **113**, 870–&.
- 60 A. Navrotsky, C. C. Ma, K. Lilova and N. Birkner, *Science*, 2010, **330**, 199–201.
- 61 J. Rossmeisl, A. Logadottir and J. K. Nørskov, *Chem. Phys.*, 2005, **319**, 178–184.
- 62 I. C. S. Man, H. Y. Calle-Vallejo, F. Hansen, H. A. Martinez, J. I. Inoglu, N. G. Kitchin, J. Jaramillo, T. F. Nørskov and J. K. Rossmeisl, *ChemCatChem*, 2011, **3**, 1159–1165.
- 63 M. T. M. Koper, *J. Electroanal. Chem.*, 2010, **660**, 254–260.
- 64 A. J. L. R. F. Bard, *Electrochemical Methods: Fundamentals and Applications*, Wiley, 2000.